atmosphere

MDPI

Article

Projecting Changes in Temperature Extremes in the Han River Basin of China Using Downscaled CMIP5 Multi-Model Ensembles

Weiwei Xiao [1,2], Bin Wang [3,*], De Li Liu [3,4,*] and Puyu Feng [3,5]

[1] School of Tourism and Environment Resources, Ankang University, Ankang 725000, Shaanxi, China; lhy_xww@aku.edu.cn
[2] Engineering Technology Research Center for Water Resource Protection and Utilization of Han River, Ankang 725000, Shaanxi, China
[3] NSW Department of Primary Industries, Wagga Wagga Agricultural Institute, Wagga Wagga, NSW 2650, Australia; puyu.feng@dpi.nsw.gov.au
[4] Climate Change Research Centre and ARC Centre of Excellence for Climate Extremes, University of New South Wales, Sydney, NSW 2052, Australia
[5] School of Life Sciences, Faculty of Science, University of Technology Sydney, PO Box 123, Broadway, Sydney, NSW 2007, Australia
* Correspondence: bin.a.wang@dpi.nsw.gov.au (B.W.); de.li.liu@dpi.nsw.gov.au (D.L.L.)

Received: 8 March 2020; Accepted: 20 April 2020; Published: 22 April 2020

Abstract: Estimating the changes in the spatial–temporal characteristics of extreme temperature events under future climate scenarios is critical to provide reference information to help mitigate climate change. In this study, we analyzed 16 extreme temperature indices calculated based on downscaled data from 28 Global Climate Models (GCMs) that were obtained from Coupled Model Intercomparison Project Phase 5 (CMIP5) under Representative Concentration Pathway (RCP) 4.5 and 8.5 scenarios in the Han River Basin (HRB). The results indicate that the downscaled data from 28 GCMs reproduced a consistent sign of recent trends for all extreme temperature indices except the DTR for the historical period (1961–2013). We found significantly increasing trends for the warm extreme indices (i.e., TXx, TNx, TX90p, TN90p, SU, TR, and WSDI) and considerably decreasing trends for the cold extreme indices (i.e., TX10p, TN10p, CSDI, FD, ID) under both the RCP4.5 and 8.5 scenarios for 2021–2100. Spatially, great changes in warm extremes will occur in the west and southeast of the HRB in the future. The projected changes in extreme temperatures will impact the eco-environment and agricultural production. Our findings will help regional managers adopt countermeasures and strategies to adapt to future climate change, especially extreme weather events.

Keywords: temperature extremes; statistical downscaling; Han River Basin; climate change; GCM; CMIP5

1. Introduction

Compared with the mean values of climate change, extreme climate events (such as floods, droughts, typhoons, storms, extreme heat, and extreme cold) are sudden, unpredictable, and highly destructive; they have a great impact on the natural system, can cause serious damage to the ecological environment and human life, and can affect global food security and water resource supplies [1–3]. Many studies have noted that increasing temperatures can alter the length of the potential growing season, accelerate phenological development and leaf senescence, and affect cropping systems and grain yield [4,5]. Meanwhile, summer heatwaves are a serious threat to human health and can even cause fatalities directly via heat-related illness [3]. Furthermore, climate warming will lead to an

increase in precipitation and evapotranspiration, resulting in a likely intensification of the hydrological cycle, causing an increased frequency of extreme climate events [6]. As extreme climate events have great adverse effects, quantifying their changing trends under future climate scenarios is essential.

Numerous studies have shown the increasing trends under extreme heat temperature events and decreasing trend during extreme cold temperatures under future climate change scenarios at different spatiotemporal levels [7–9]. However, the complexity of extreme temperature events is indicated by their regional differences in space and their multiple temporal scales. The amount of the increase or decrease of projected future extreme temperatures depends on the study areas, the selected Global Climate Models (GCMs), and future emission scenarios. For example, the observed global mean warming of 0.85 °C has increased the probability of "1-in-1000-day" hot extremes over the land by a factor of five compared to pre-industrial conditions [2]. In the United States, Schoof and Robeson [10] reviewed historical changes and projected the future changes of temperature extremes; their results showed an obvious growing trend of warm extremes and a decreasing trend of cold extremes throughout the domain. Alexander and Arblaster [11] reported that the days below freezing in Australia would decrease coincidently with an increase in daily minimum temperatures. Nikulin, et al. [12] noted that the cold extremes in central Europe would become warmer due to strong increases in winter's minimum temperatures. However, these warm extremes will intensify over all of Europe by the end of this century.

In China, Shi, et al. [13] found that the increases in temperature extremes over China are larger than those on a global scale. Strongly growing trends for warm extremes and considerably declining trends for cold extremes were recorded in most of mainland China [14]. Yang, et al. [15] projected an upward trend in temperature extremes for all seasons in the subtropical region of southern China. Here, the mixing of moist warm air and dry cold air originating from northern China releases excessive torrential rains in this basin. The spatiotemporal changes of extreme temperature indices may have many impacts on agricultural production, such as variety adaptability, the shifting of cultivation, and crop yields in different climatic zones in China [16]. He, et al. [17] predicted rice heat stress indices in southern China using the statistical downscaling method with 28 GCMs from 2061 to 2100 under RCP4.5 and RCP8.5 and they found that the projected heat stress frequency in rice-growing areas increased to a growing trend.

At the same time, numerous studies on changes in climate extremes have been conducted over several key basins for ecological security in China, including the Yellow River Basin [18], Yangtze River Basin [19], Three-Rivers Headwater Region [20], Pearl River Basin [21], and Wei River Basin [22]. These special areas are becoming more vulnerable and sensitive to climate change, especially to extreme and severe weather. However, the magnitudes of extreme climate events vary over climate scenarios and geographic regions. These previous studies provide a reference basis for local decision-making and planning to adapt to climate change [23].

Estimating the future potential changes in temperature extremes can provide adaptation and planning strategies to face disasters. Climate system models have been used to simulate and predict future climate changes [24]. Many projections of future temperature extremes have been developed based on different GCMs and different scenarios [9,11,20,25,26]. Generally, most models show good ability to capture the basic changing trends and spatial differences. However, due to the bias and coarse spatial resolution of GCMs (200–500 km), it remains difficult to reasonably predict the climate response of a given scenario on a regional scale, especially for sub-continental regions [27,28]. Downscaling methods can efficiently improve the resolution and obtain site-specific climate data [29]. The downscaling method was performed based on the established relationships between historical observed weather records from meteorological stations to re-analyze large scale atmospheric predictors.

There are two different methods used for downscaling the GCM data: dynamic downscaling and statistical downscaling. Although dynamical downscaling can generate higher spatial resolutions using Regional Climate Models (RCMs), it requires serious computational power and strongly relies on the boundary conditions provided by GCMs [15]. Statistical downscaling has become

a popular approach to gain site-scale data [30], and site-scale changes can always provide more reliable results on the appearance and disappearance of extremes than grid-scale changes [31]. Some scholars have used statistical downscaling to conduct studies on the temperature extremes in different regions [5,10,15,17,31–33]. In these studies, downscaled GCM outputs performed well in reproducing temperature extremes and providing reliable results on the appearance and disappearance of extremes. However, due to the great differences in climate backgrounds and regional environmental features, the variability of climatic extremes tends to be different in different climate regions. Thus, a comprehensive analysis of extreme temperature events should be conducted in different regions using multiple GCMs under multi-emission scenarios with more climate change core indices to deepen our understanding of extreme temperature events in different climate regions of China under the background of global warming.

The Han River is the longest tributary of the Yangtze River, located at an important climate transition zone in China; this tributary is extremely sensitive and fragile to global climate change. As the main grain-yielding and most important point of economic transmission in the central and western regions of China, the economic development of the Han River Basin (HRB) occupies an important position in the Yangtze River Basin and for the whole country. Moreover, the HRB is the most important source of water for the Middle Route Project of the South-to-North Water Transfer Project in China, which directly supports the production and livelihoods of 438 million people [34].

In general, dynamic change of extreme temperature under the background of global climate change will have an important impact on the natural, social, and economic security of this region. Ren and Yin [35] noted that the annual average temperature and annual average minimum temperature increased in the upper reaches of the Han river during 1960–2010. The spring coldness and autumn disasters caused serious damage to crop production. By analyzing the extreme temperature of Ankang city in Han River during the historical period, Zhao et al. [36] found that the warm extremes were increased and cold extremes were decreased. Changes in extreme temperatures will lead to an increasing trend of drought, high temperatures, agricultural pests, and diseases in this region. Xiang et al. [37] reported that the positive correlation trend between the extreme temperature indices and altitudes is significant in the upper reaches of the Han River. To date, most previous studies on climate change in the HRB have focused on mean temperature changes only in parts of the HRB or in certain historical periods. Studies on the future spatial–temporal changes of extreme temperature events across the whole HRB have not been conducted.

The main purposes of this study were to utilize observed and projected future climate data to (1) analyze the historical trends of temperature extremes during 1961–2013 based on 16 extreme temperature indices recommended by the Expert Team on Climate Change Detection and Indices (ETCCDI) in the HRB; (2) to present the spatiotemporal patterns of changes in these selected extreme temperature indices during the future period during 2021–2100 based on 28 CMIP5 GCMs under RCP4.5 and 8.5 emission scenarios in the HRB.

2. Data and Methods

2.1. Study Area

The Han River (30°8′–34°11′ N, 106°12′–114°14′ E) originates from the Ningqiang County of Shaanxi province, which is located in the middle of China (Figure 1). The river is 1577 km in length and covers an area of approximately 1.5×10^5 km^2. The Han River flows through 14 cities of Shaanxi and Hubei provinces and is an extremely important water resource for industrial and agricultural production and people's livelihoods in Shaanxi and Hubei provinces. The HRB is characterized by its north sub-tropic monsoon climate. The average annual temperature ranges from 12 to 16 °C, with a maximum temperature of about 43 °C and a minimum temperature of about −13 °C, respectively. The average annual precipitation is approximately 800 mm, and 70%–80% of the rainfall occurs from May to October in the rainy season [38]. As one of the most important granaries in China, the grain

production of the HRB not only guarantees the subsistence and development of tens of millions of people in the basin but also occupies a prominent position in the national strategy of grain production. In the future, it will play a more important role in China's food security, ensuring social stability and sustainable development [39].

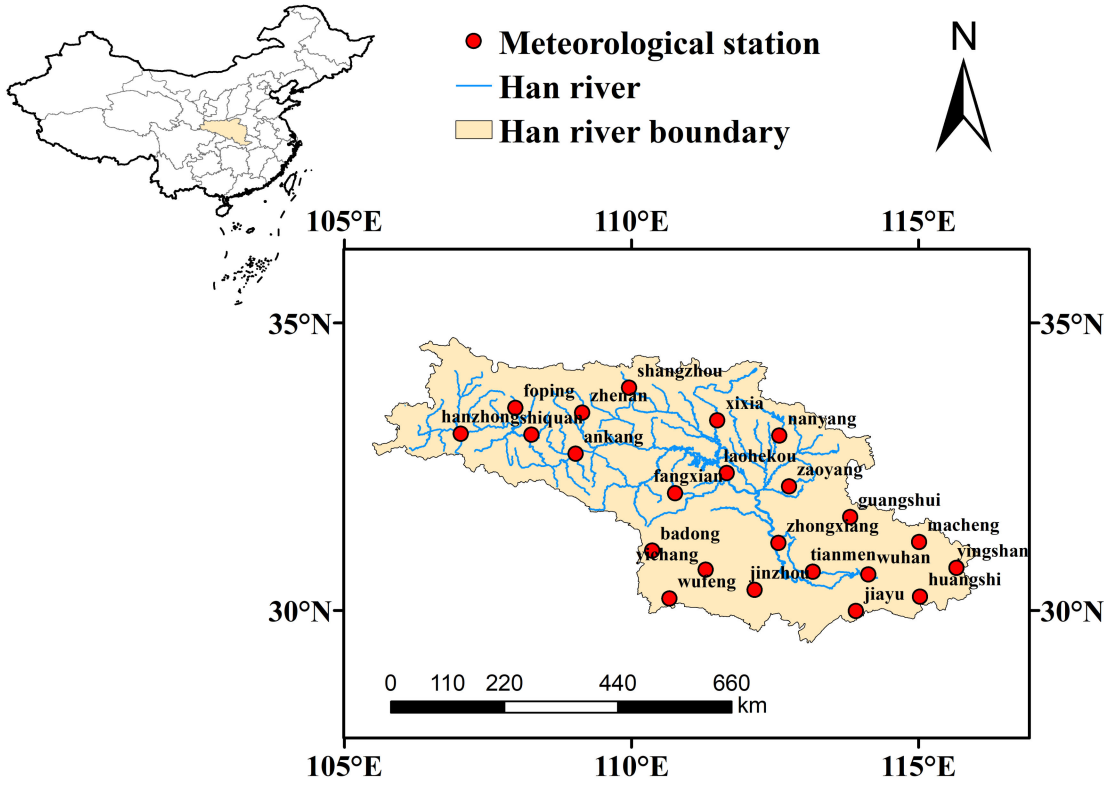

Figure 1. Locations of the study area and the distribution of meteorological stations.

2.2. Climate Data

In this study, observed daily T-max and T-min data from 1961 to 2013 at 23 meteorological stations were collected from the China Meteorological Administration (http://www.nmic.gov.cn/). The information on the 28 selected CMIP5 models used to project the changes in extreme temperature indices is shown in Table 1. A statistically-downscaled model (NWAI-WG) developed by Liu and Zuo [40] was used to generate the monthly data on each GCM grid for the daily climate data at each station. A bias correction and uncertainty test for this method, carried out by Liu and Zuo [40], showed that the observed daily, monthly, and annual climate variables can be reproduced well by the downscaling model. The NWAI-WG downscaling procedure has been used in many studies in different regions and has been proven to be efficient at correcting the bias of GCM data and simulating future climate changes [5,16,17,41]. In short, the first step of this method is spatial downscaling. We downscaled the monthly GCM simulations data to specific sites, followed by a bias-correction of the simulated GCM monthly values to match the observed data using the qq-mapping technique. The second step involves temporal downscaling. The monthly data of specific sites were disaggregated to daily data through a modified WGEN stochastic weather generator. More details of this procedure can find in the article by Liu and Zuo [40].

Table 1. Information on the 28 CMIP5 models used in the study.

Model Name	Abbreviation of GCM	Institution/Country
BCC-CSM1.1	BC1	BCC/China
BCC-CSM1.1(m)	BC2	BCC/China
BNU-ESM	BNU	GCESS/China
CanESM2	CaE	CCCMA/Canada
CCSM4	CCS	NCAR/USA
CESM1(BGC)	CE1	NSF-DOE-NCAR/USA
CMCC-CM	CM2	CMCC/Europe
CMCC-CMS	CM3	CMCC/Europe
CSIRO-Mk3.6.0	CSI	CSIRO-QCCCE/Australia
EC-EARTH	ECE	EC-EARTH/Europe
FIO-ESM	FIO	FIO/China
GISS-E2-H-CC	GE2	NASA GISS/USA
GISS-E2-R	GE3	NASA GISS/USA
GFDL-CM3	GF2	NOAA GFDL/USA
GFDL-ESM2G	GF3	NOAA GFDL/USA
GFDL-ESM2M	GF4	NOAA GFDL/USA
HadGEM2-AO	Ha5	NIMR/KMA Korea
INM-CM4	INC	INM/Russia
IPSL-CM5A-MR	IP2	IPSL/France
IPSL-CM5B-LR	IP3	IPSL/France
MIROC5	MI2	MIROC/Japan
MIROC-ESM	MI3	MIROC/Japan
MIROC-ESM-CHEM	MI4	MIROC/Japan
MPI-ESM-LR	MP1	MPI-M/Germany
MPI-ESM-MR	MP2	MPI-M/Germany
MRI-CGCM3	MR3	MRI/Japan
NorESM1-M	NE1	NCC/Norway
NorESM1-ME	NE2	NCC/Norwa

2.3. Extreme Temperature Indices

In this study, we adopted 16 extreme temperature indices identified by ETCCDI (http://etccdi.pacificclimate.org), which are widely adopted and recognized. For comparison purposes, we classified these indices into four groups: four intensity-based extreme temperature indices, four percentile-based indices, four spell duration indices, and four fixed threshold-based indices. Intensity-based extreme temperature indices included the warmest day (TXx), warmest night (TNx), coldest day (TXn), and coldest night (TNn). Percentile-based indices included warm days (TX90p), warm nights (TN90p), cold days (TX10p), and cold nights (TN10p). Spell duration indices included the warm spell duration index (WSDI), cold spell duration index (CSDI), growing season length (GSL), and daily temperature range (DTR). Fixed threshold-based indices included the number of summer days (SU), number of tropical nights (TR), number of icing days (ID), and number of frost days (FD). The details of the 16 extreme indices are shown in Table 2. In this study, 16 extreme temperature indices were calculated by using the NWAI-WG statistically downscaled T-max and T-min data. The R software package 'climdex.pcic' was used to calculate the extreme temperature indices.

Table 2. Information on the climate extreme indices analyzed in this study. All indices were calculated annually.

Label	Description	Unit
	Intensity-based Extreme Temperature Indices	
TXx	maximum value of daily T-max	°C
TNx	maximum value of daily T-min	°C
TXn	minimum value of daily T-max	°C
TNn	minimum value of daily T-min	°C
	Percentile-based Indices	
TN10p	Annual count when T-min < 10th percentile of 1961–1990	days
TX10P	Annual count when T-max < 10th percentile of 1961–1990	days
TN90P	Annual count when T-min > 90th percentile of 1961–1990	days
TX90P	Annual count when T-max > 90th percentile of 1961–1990	days
	Fixed threshold-based Indices	
FD	Annual count when daily minimum temperature < 0 °C	days
TR	Annual count when daily min temperature > 25 °C	days
SU	Annual count when daily max temperature > 25 °C	days
ID	Number of days when the daily maximum temperature < 0 °C	days
	Spell Duration Indices	
GSL	Growing season length	days
WSDI	Annual count when at least 6 consecutive days of max temperature > 90th percentile of 1961–1990	days
CSDI	Annual count when at least 6 consecutive days of min temperature < 10th percentile of 1961–1990	days
DTR	Difference between daily max and min temperature	°C

2.4. Statistical Analysis

The nonparametric Mann–Kendall (MK) test, which is recommended by the World Meteorological Organization (WMO), is a useful method to infer the level of significance of trends [42,43]. It has been widely applied to detect changes in climatic and hydrologic time series, such as temperature, precipitation, stream flow, and water quality. In general, the Z value represents the level of significance. Positive Z values indicate increasing trends, and negative Z values indicate decreasing trends. When $|Z| > 1.96$, the trend's significance is at a 95% confidence level, and at a 99% confidence level if $|Z| > 2.58$. Sen's estimator of slope [44] can be used to estimate the magnitude of trends. In this study, the MK test was used to detect the stability of trends and the statistical significance in the time series of the extreme temperature indices. Temporal changes in the future were quantified by the downscaled multi-model ensemble means of two 40-year time slices: the 2040s (2021–2060) and the 2080s (2061–2100).

In this study, the arithmetic mean (AM) value of 28 GCM-based extreme temperature indices was calculated to compare with the observation data. The regional averages were the arithmetic mean values of all selected stations. The linear tendency estimation method was used to analyze the trends of the extreme temperature indices. To analyze the spatial distributions of the temperature extremes, the inverse distance weighting (IDW) method was used to draw spatial trend maps in ArcGIS.

3. Results

3.1. Comparison between Observed and Projected Temperature Extremes during the Historical Period

In this section, we investigated how well the GCM ensemble and its individual members can reproduce the temperature extremes in the HRB during the historical period (1961–2013). The projected results were compared with the observed data (Figure 2). There were significant increasing trends for the observed warm extremes indices (TNx, TNn, TXn, TX90p, TN90p, WSDI, TR, and SU), while significant decreasing trends were found for the cold extremes indices (TX10p, ID, and FD). Both the observed and GCM-based extreme temperature indices showed large interannual variability over the historical period. As a result of the positive and negative biases in the individual GCMs, the multi-model mean showed almost no significant differences compared to the observed data over this region (Figure 2). Moreover, the AM value from 28 GCMs had less variability than individual models and observations because of its averaged nature, leading to a significant trend for all extreme temperature indices except DTR. The trends of DTR were insignificant and inconsistent between observed and projected trends. The annual extreme temperature indices based on observed and 28 GCMs data were paired according to their rank and plotted to yield a q-q plot (see Supplementary Material Figure S1). The bias-corrected GCM projected annual extreme temperature indices in the period of 1961–2013 were fairly close to the observed annual indices, except for WSDI. This is because the WSDI is a weather-based index. The observed climate data represent the weather sequences but GCM projected data represent long-term climate projections. This means the q-q plot comparison is under different climate scales, i.e., weather-based vs climate-based index. Overall, the results indicate that the AM simulations can rationally reproduce the variations and trends of extreme temperature indices. For instance, the observed TN90p increased by 1.7 days/decade, while the AM value increased by 28 GCMs, and TN90p increased by 1.8 days/decade from 1961 to 2013.

The root-mean-square error (RMSE) values were calculated between the observations and the AM, as well as between the 28 individual GCMs. For each extreme temperature index, the AM values usually had smaller RMSE values than the individual GCMs, except for ID and WSDI from 1961 to 2013 (Table 3).

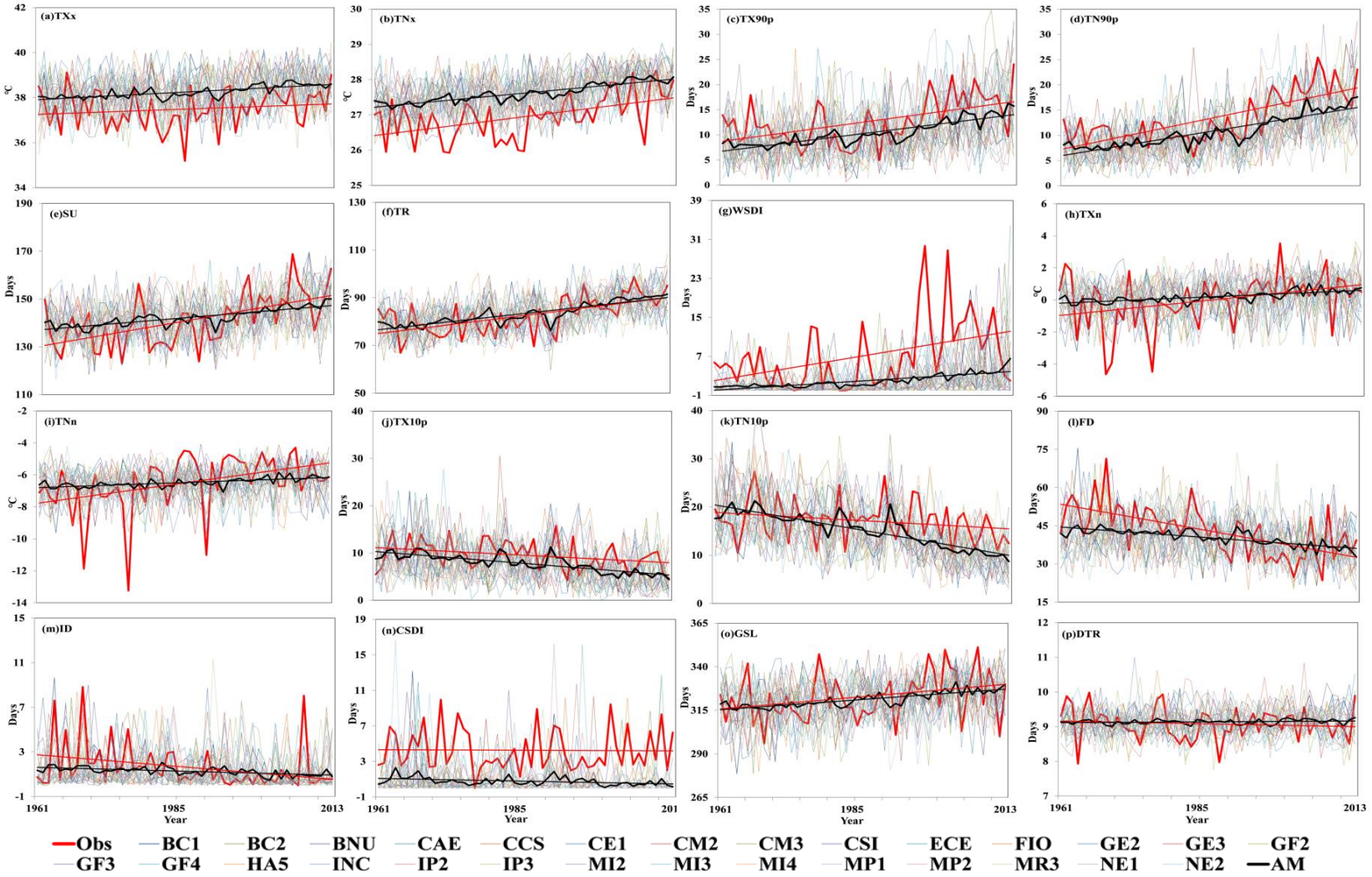

Figure 2. Time series of the observed values (red line) and 28 Global Climate Models (GCM) simulations, including the multi-model average mean (AM, black line) extreme temperature indices during 1961 to 2013 across the Han River Basin.

Table 3. Root mean square error (RMSE) between the muti-model arithmetic mean for each GCM and observed values for the 16 temperature indices during 1961–2013.

GCMs	TXx	TNx	TXn	TNn	TN10p	TX10P	TN90P	TX90P	FD	TR	SU	ID	GSL	WSDI	CSDI	DTR
BC1	1.346	0.969	1.879	1.975	4.513	4.878	5.254	5.449	12.233	8.638	12.173	2.113	18.575	8.494	3.127	8.638
BC2	1.519	0.993	2.054	1.885	4.466	5.409	5.220	6.384	10.310	8.839	12.851	2.455	15.122	8.628	3.231	8.839
BNU	1.326	0.963	1.693	1.762	3.864	4.707	5.216	5.824	10.900	8.956	12.418	2.159	16.523	8.894	2.746	8.956
CAE	1.351	0.983	1.916	1.914	4.652	4.912	5.333	4.951	11.508	7.077	10.532	2.397	18.021	8.439	2.994	7.077
CCS	1.397	0.981	1.857	1.750	4.639	5.795	6.386	6.722	11.459	8.338	9.989	2.625	18.955	8.969	3.021	8.338
CE1	1.473	1.072	2.131	1.954	4.265	4.754	4.986	6.208	13.614	10.096	11.054	2.622	18.454	8.654	3.003	10.096
CM2	1.365	1.002	1.945	1.957	4.599	5.317	5.933	5.922	11.380	7.220	10.524	2.583	17.501	9.157	3.023	7.220
CM3	1.375	1.023	1.788	1.739	3.859	5.008	5.226	7.730	10.601	8.312	10.645	2.449	17.860	9.151	3.338	8.312
CSI	1.442	0.968	1.879	1.834	3.483	5.566	6.961	7.502	10.995	8.667	13.415	2.310	13.907	9.220	2.861	8.667
ECE	1.417	1.071	1.828	1.876	3.733	4.991	5.699	6.316	12.342	8.589	14.148	2.314	16.519	10.014	3.061	8.589
FIO	1.439	0.999	1.978	1.909	4.565	4.729	5.764	5.823	12.537	8.616	11.793	2.566	18.824	8.426	3.091	8.616
GE2	1.362	1.042	1.813	1.835	4.090	4.210	5.168	5.703	12.436	8.671	10.467	2.576	17.770	8.736	3.019	8.671
GE3	1.313	0.941	1.746	1.982	3.982	5.770	5.378	5.690	11.612	7.416	11.992	1.938	17.523	8.994	3.361	7.416
GF2	1.301	0.937	2.124	2.009	3.950	5.158	6.397	6.703	14.283	7.592	11.368	2.629	20.630	9.607	2.858	7.592
GF3	1.431	0.967	1.955	2.068	3.954	4.945	5.275	4.991	11.313	7.769	11.925	2.463	17.325	8.750	3.086	7.769
GF4	1.431	1.008	1.936	2.036	4.375	5.399	5.896	6.623	11.487	8.446	10.503	2.527	16.480	8.168	3.034	8.446
HA5	1.086	0.899	1.929	1.937	4.100	5.486	6.969	6.736	12.396	8.855	10.604	2.540	16.189	9.347	2.700	8.855
INC	1.416	1.012	1.973	2.118	3.324	5.651	4.956	6.854	11.536	8.762	12.293	2.547	14.542	7.817	2.668	8.762
IP2	1.349	0.908	1.956	1.855	4.021	4.403	6.039	6.843	11.084	6.359	11.552	2.454	16.072	9.115	3.154	6.359
IP3	1.400	0.981	1.793	1.793	4.317	5.159	6.058	7.353	10.785	7.522	12.405	2.497	14.169	9.335	2.918	7.522
MI2	1.463	0.944	1.864	2.063	3.572	4.301	5.613	6.912	11.666	7.749	12.220	2.566	17.032	8.417	2.813	7.749
MI3	1.340	0.965	1.869	1.908	4.972	6.451	6.333	6.934	11.309	8.441	13.390	2.346	15.773	8.266	4.081	8.441
MI4	1.456	1.075	2.182	2.037	4.356	5.644	4.930	5.040	13.779	8.998	12.956	2.797	18.698	7.932	3.038	8.998
MP1	1.410	0.962	2.174	1.749	3.800	4.831	5.563	6.172	12.897	8.713	10.323	2.593	16.810	8.180	2.979	8.713
MP2	1.354	1.004	1.872	2.060	4.256	4.626	6.161	7.273	11.576	7.705	11.191	2.373	16.017	9.655	3.092	7.705
MR3	1.449	0.978	1.993	1.924	4.082	4.444	5.082	6.587	11.861	9.295	13.798	2.973	15.935	8.860	3.085	9.295
NE1	1.401	0.963	1.850	1.982	4.585	5.269	5.544	6.568	10.028	9.301	10.986	2.284	15.548	8.951	3.070	9.301
NE2	1.306	0.948	1.981	2.079	4.823	5.103	5.757	5.892	12.734	9.233	11.176	2.642	15.935	9.092	3.540	9.233
AM	**1.108**	**0.847**	**1.569**	**1.686**	**2.475**	**3.279**	**4.044**	**4.260**	**8.926**	**5.664**	**8.930**	**2.007**	**12.359**	**8.292**	**2.570**	**5.664**

3.2. Projected Changes of Temperature Extremes by Multi-Model Ensembles in the Future

The spatial changes of the multi-model ensemble simulated extreme temperature indices between the baseline (1971–2010) and two future periods (the 2040s and 2080s) under the RCP4.5 and 8.5 scenarios are shown in Figures 3–6. The temporal changes of the extreme indices across the HRB during 1961 to 2100 under the two scenarios for the AM results are shown in Figure 7. As shown in Figures 3–7, all temperature indices, except DTR, featured a significant increasing trend under RCP4.5 and RCP 8.5 during the 21st century, and the temperature indices under the RCP 8.5 scenarios increased faster than those under RCP 4.5 scenarios in all periods.

3.2.1. Projected Changes in the Four Intensity-Based Extreme Indices (TXx, TNx, TNn, TXn)

Compared with the baseline period (1971–2010), a significant growing trend was detected in the T-max and T-min indices in the next two periods (Figure 3). During 2021 to 2060, the rise in TXx and TNx across the whole basin will be 0.3–2.9 °C and 0.3–1.8 °C under RCP4.5 and 1.0–3.9 °C and 2.4–5.8 °C under RCP8.5. The increase of TXn was the most significant in the east, with a range of −0.7–2 °C under RCP 4.5 and −0.4–3.3 °C under RCP8.5, respectively. TNx and TNn revealed distinctive regional patterns, with lower values in the south than those in the north along the latitude, especially for TNn in the southwest in the ranges of 0.0–1.3 °C and 0.3–2.2 °C under RCP 4.5 and 8.5, respectively.

By the end of the 21st century (2061–2100), the spatial distribution characteristics are projected to be generally similar to those from 2021 to 2060, but the increased magnitude is greater. For example, the TXx in the 2080s will increase by about 0.7–1 °C more than the TXx in the 2040s under RCP4.5 and will increase by about 1.4–1.9 °C more than the increase in the 2040s under RCP8.5. TNx showed the largest increases in the west of about 0.9–2.4 °C under RCP4.5 and 2–3.8 °C under RCP8.5, respectively. For TXn, the most significant increases in the east were −0.7–2 °C under 4.5 and −0.4–3.3 °C under RCP8.5. However, TNn shows a great potential increase in the east in the 2080s (0.3–1.3 under RCP4.5 and 0.7–2.2 °C under RCP8.5).

For the area-averaged TXx, TNx increased by 0.2–0.1 °C /decade for RCP4.5 and 0.5–0.4 °C /decade for RCP8.5, while for the area-averaged TXn, TNn increased by 0.2–0.1 °C/decade for RCP4.5 and 0.4–0.2 °C/decade for RCP8.5, respectively. The significant increases over time were distributed in the western study area.

3.2.2. Projected Changes in the Four Percentile-Based Indices

Compared to the baseline period, the cold days of TX10p and cold nights of TN10p showed a downward trend while the warm days of TX90p and warm nights of TN90p gradually increased (Figure 4). A considerable increase was found in the east for TX90p from 15 to 30 days and for TN90p from 17 to 34 days under RCP4.5, as well as for TX90p from 19 to 45 days and for TN90p from 21 to 54 days under RCP8.5. During 2021–2100, TX90p showed a significant increasing trend of 2.3 d/decade ($p < 0.01$) and 5.5 d/decade ($p < 0.01$) for RCP4.5 and RCP8.5, respectively. TN90p increased at a rate of 2 d/decade ($p < 0.01$) and 5 d/decade ($p < 0.01$) for RCP4.5 and RCP8.5, respectively. TX10p was projected to decrease by about 1–9 d for RCP4.5 and by about 2–13 d for RCP8.5. TN10p presented a similar changing pattern, decreasing at a range of 2–10 d for RCP4.5 and 4–14 d for RCP8.5. TX10p andTN10p had consistent decreasing trends at 0.56 and 0.62 d/decade ($p < 0.01$) for RCP4.5 and 0.84 and 0.99 d/decade ($p < 0.01$) for RCP8.5.

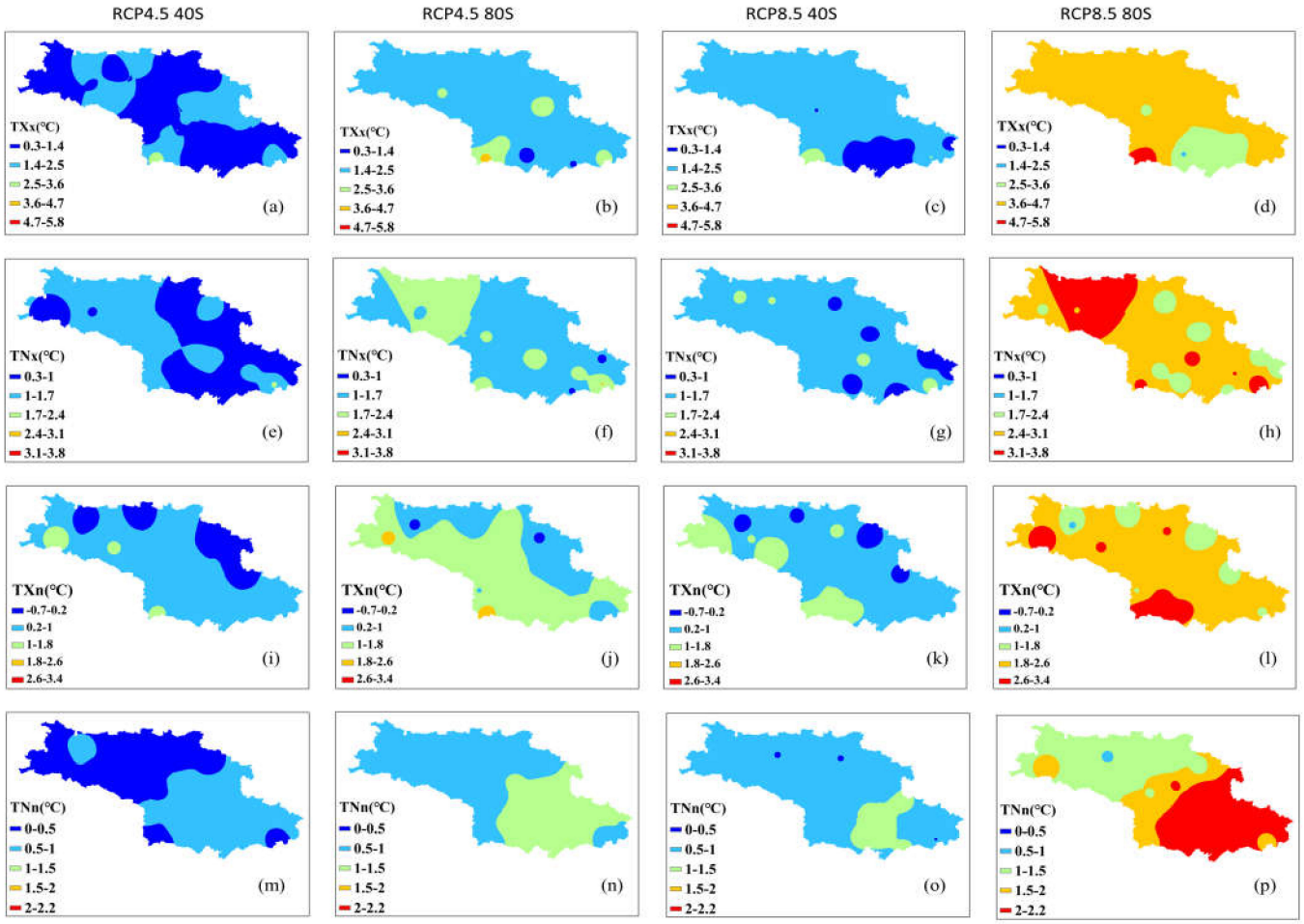

Figure 3. The spatial distribution of changes in the multi-model ensemble for the four intensity-based extreme indices (TXx, **a**–**d**; TNx, **e**–**h**; TXn, **i**–**l**; TNn **m**–**p**) during the 2040s and 2080s under two scenarios relative to 1971–2010 across the Han River Basin.

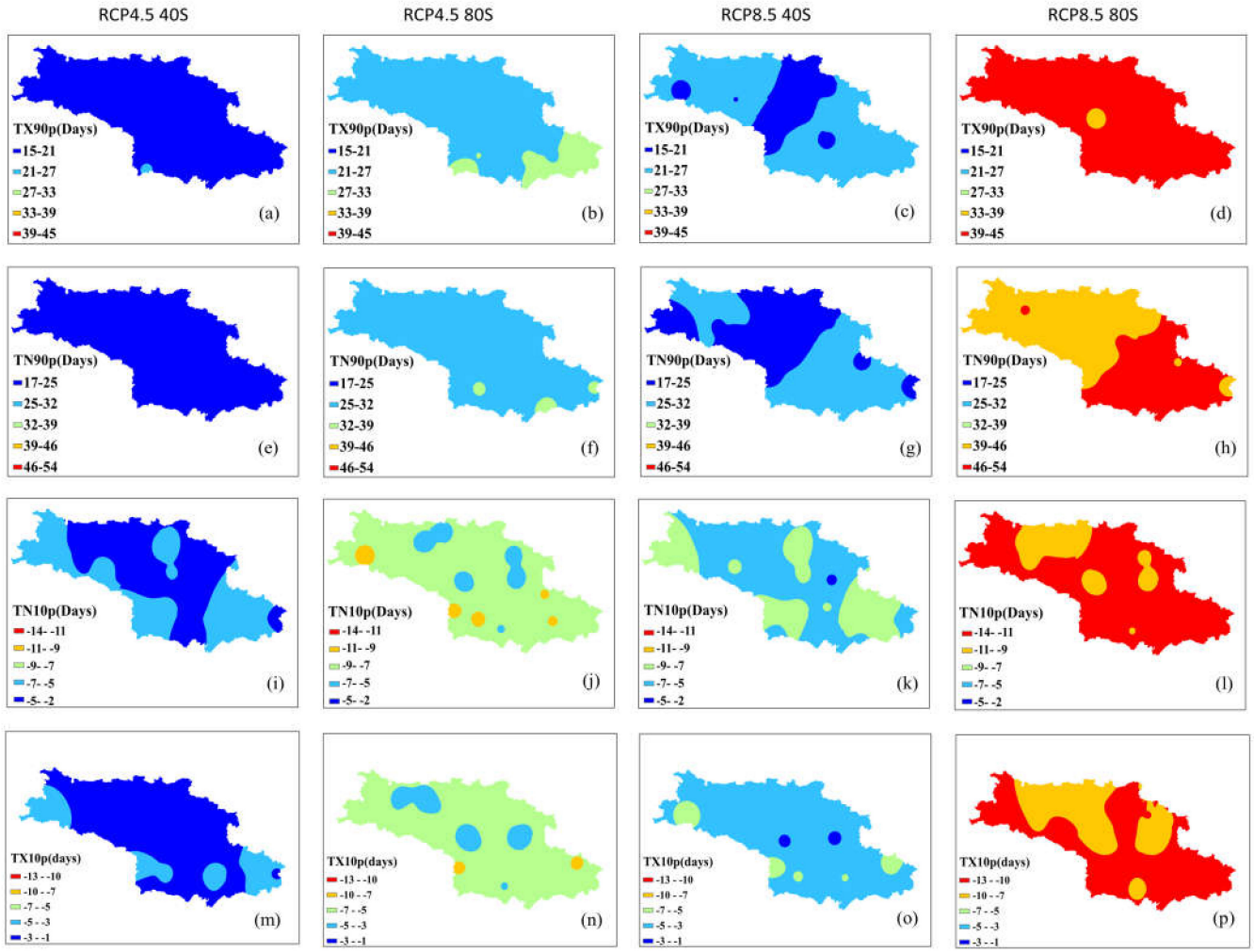

Figure 4. The spatial distribution of changes in the multi-model ensemble for the four percentile-based indices (TX90p, **a**–**d**; TN90p, **e**–**h**; TN10p, **i**–**l**; TX10p **m**–**p**)during the 2040s and 2080s under two scenarios relative to 1971–2010 across the Han River Basin.

3.2.3. Projected Changes in Four Spell Duration Indices

WSDI is an index that handles consecutive high temperatures and is an important indicator of heatwaves. The WSDI increased significantly in the east under two scenarios (Figure 5a–d). During 2021–2100, WSDI will increase by 4.5 d/decade ($p < 0.01$) and 16.1 d /decade ($p < 0.01$) for RCP4.5 and RCP8.5, respectively. CSDI presented a consistent decreasing trend at 0.4 d/decade ($p < 0.01$) and 0.3 d/decade ($p < 0.01$) for RCP4.5 and RCP8.5, respectively (Table 4). In HRB, all GCM models projected that the CSDI at most sites will decrease to zero, indicating that the models reached a consensus result that there will be no CSDI at these sites towards the end of the 21st century.

The growing season length (GSL) in the HRB region was shown to increase at a rate of 1.8 days/decade ($p < 0.01$) and 3 d/decade ($p < 0.01$) for RCP4.5 and RCP8.5, respectively (Figure 5i–l). The largest increase is concentrated in the north and south regions of the HRB. Notably, the growing season might increase by about 45 days in the northern regions by the end of this century under RCP8.5. Over 2021–2100, the Diurnal Temperature Range (DTR) increased at a rate of 0.04 °C/decade ($p < 0.01$) and 0.1 °C/decade ($p < 0.01$) under RCP4.5 and RCP8.5, respectively (Table 4). Significant increases were concentrated in the western study area. Furthermore, in the 2080s, the spatial distribution characteristics will generally be similar to those in 2040s, but the amount of this increase will be greater (Figure 5m–p).

3.2.4. Future Changes in Four Fixed Threshold-Based Indices

Another significant type of warming in the HRB is reflected by the four fixed threshold-based indices (Figure 6a–p). There is an obvious upward trend for SU and TR over the whole basin, while the annual FD gradually decreases in the north. SU and TR both increase by 2.3 d/decade ($p < 0.01$) and 5.8 d/decade ($p < 0.01$) for RCP4.5 and RCP8.5, respectively. However, the previously rapid increase slowed and maintained a high range from 2021 to 2100. The obvious increases over time were mainly distributed to the north of the HRB.

FD showed a significant downward trend at 1.3 d/decade ($p < 0.01$) and 2.4 d/decade ($p < 0.01$) for RCP4.5 and RCP8.5, respectively. ID (days with T-max < 0 °C) may disappear by the 2040s (2021–2060), which means that the daily maximum temperature of the HRB would always remain above 0 °C from the 2040s onward. Some of the threshold-based indicators, such as ID, are relatively rare in the HRB, so not all ETCCDI indicators apply to all regions.

As shown in Figure 7, the time series for the 16 extreme temperature indices showed similar features, characterized by increases and no distinguishable differences between RCP4.5 and 8.5 before 2060. However, after the year 2060, increases in the warm extreme indices slowed down under RCP 4.5 scenarios (Table 4).

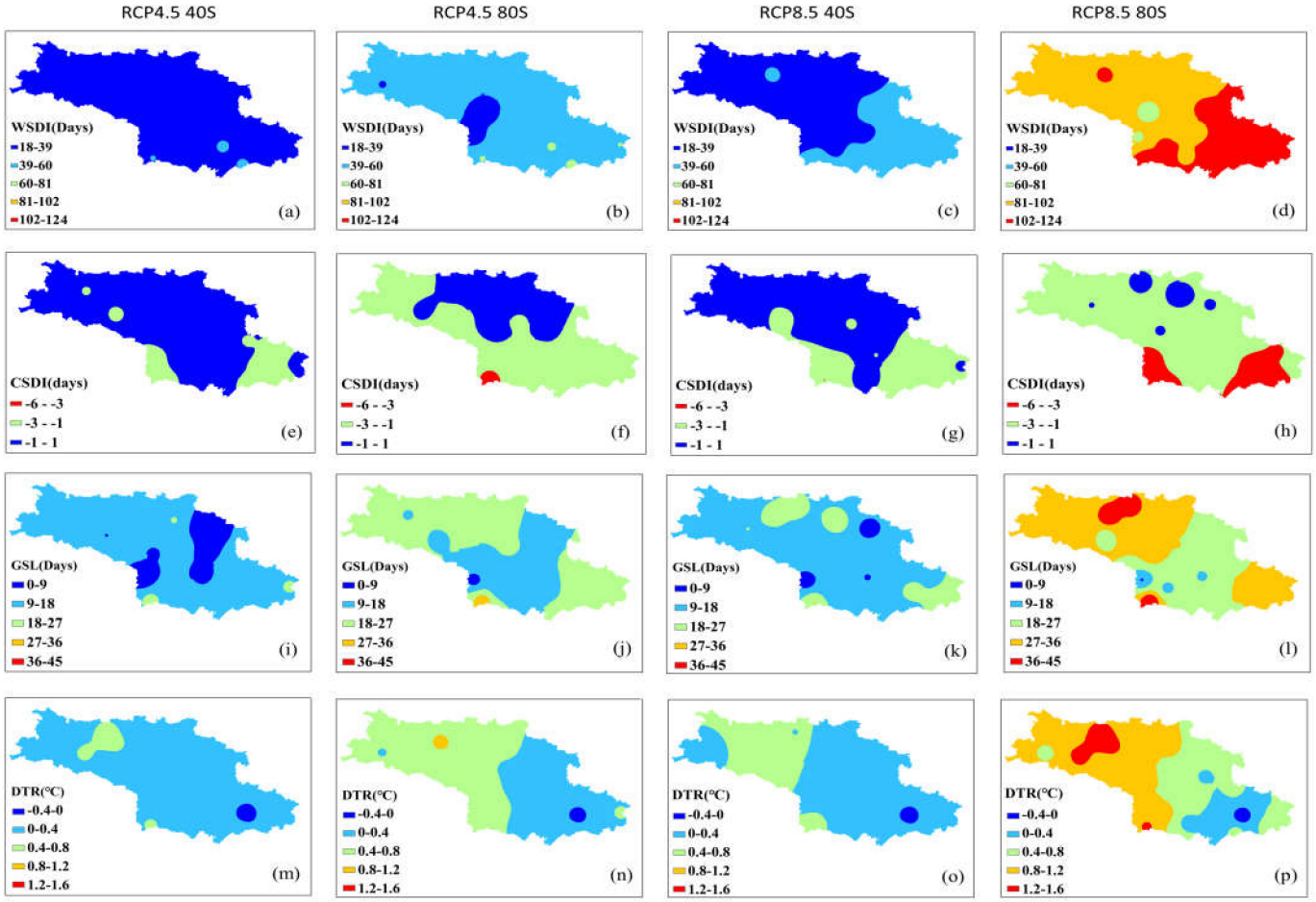

Figure 5. The spatial distribution of changes in the multi-model ensemble for the four spell duration indices (WSDI, **a**–**d**; CSDI, **e**–**h**; GSL, **i**–**l**; DTR **m**–**p**) during the 2040s and 2080s under two scenarios relative to 1971–2010 across the Han River Basin.

Table 4. Trends of the multi-model arithmetic mean for the 16 temperature indices during 2021–2100 under the two scenarios. * $p < 0.05$, ** $p < 0.01$.

Time Period	RCPS	TXx	TNx	TXn	TNn	TN10p	TX10P	TN90P	TX90P	FD	TR	SU	ID	GSL	WSDI	CSDI	DTR
2021–2060	4.5	0.0313**	0.0212**	0.0231**	0.0136**	−0.101**	−0.1125**	0.3471**	0.3155**	−0.1939**	0.3669**	0.3756**	−0.0167**	0.2687**	0.6371**	−0.0693**	0.0082**
	8.5	0.0476**	0.0341**	0.0334**	0.0188**	−0.1209**	−0.138**	0.5696**	0.5005**	−0.269**	0.6083**	0.5827**	−0.0188**	0.3674**	1.1724**	−0.0599**	0.0105**
2061–2100	4.5	0.0077**	0.0059**	0.011**	0.0069**	−0.0214**	−0.0191**	0.1149**	0.0952**	−0.0697**	0.097**	0.0947**	−0.007**	0.0847**	0.2433**	−0.0104*	0.001
	8.5	0.0575**	0.0376**	0.0331**	0.0217**	−0.0443**	−0.0578**	0.4913**	0.4776**	−0.1856**	0.5421**	0.6095**	−0.0044**	0.2113**	2.03**	−0.0074**	0.0116**
2021–2100	4.5	0.0202**	0.0136**	0.016**	0.0111**	−0.0564**	−0.0623**	0.2278**	0.2033**	−0.1314**	0.2329**	0.233**	−0.0131**	0.1776**	0.4501**	−0.0397**	0.0046**
	8.5	0.0528**	0.0369**	0.0357**	0.0222**	−0.0842**	−0.0992**	0.5521**	0.4974**	−0.2423**	0.5814**	0.5801**	−0.0112**	0.3026**	1.6097**	−0.03**	0.0106**

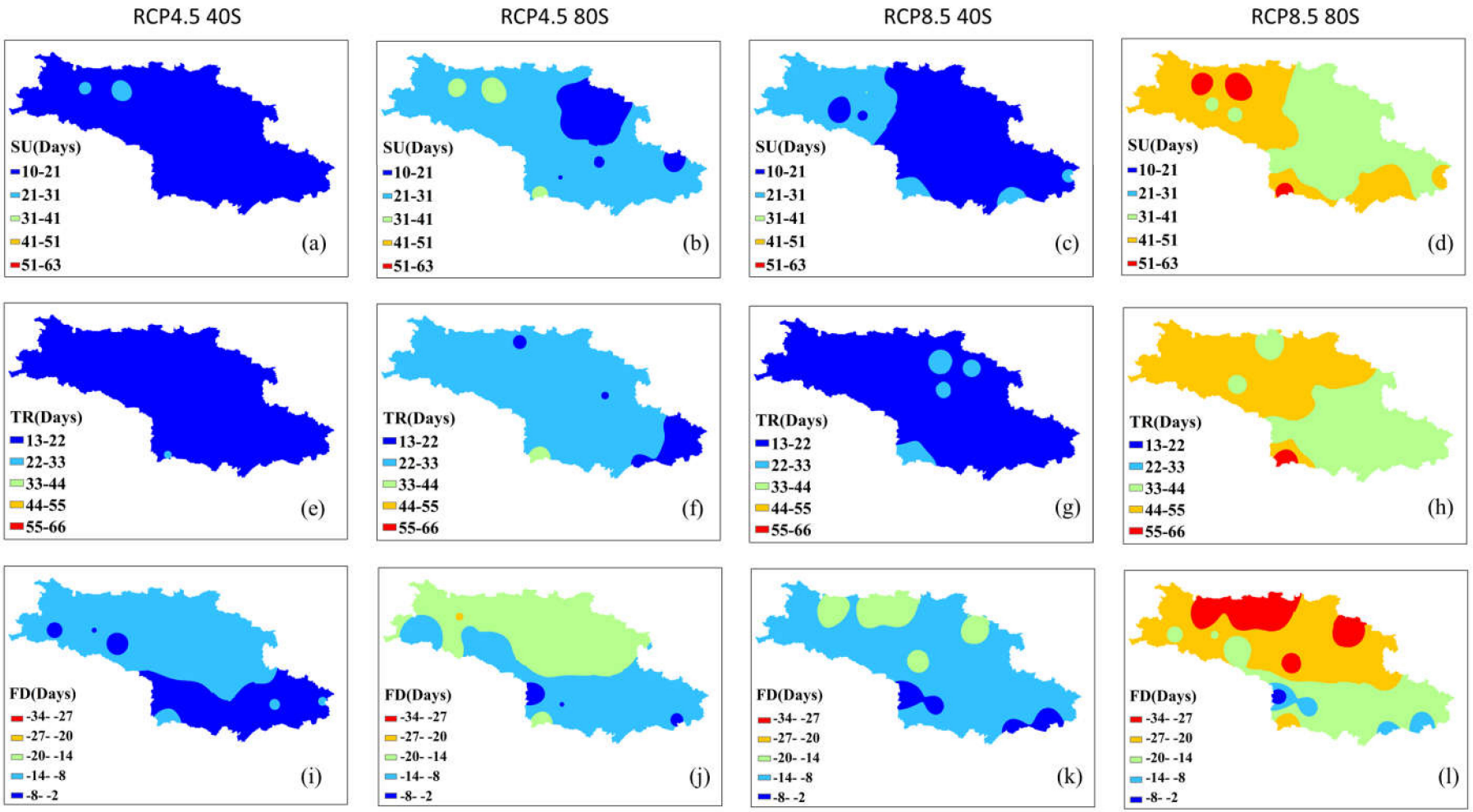

Figure 6. The spatial distribution of changes in the multi-model ensemble for the three fixed threshold-based indices (SU, **a**–**d**; TR, **e**–**h**; FD, **i**–**l**) during 2021–2100 under two scenarios relative to 1961–2013 across the Han River Basin (HRB).

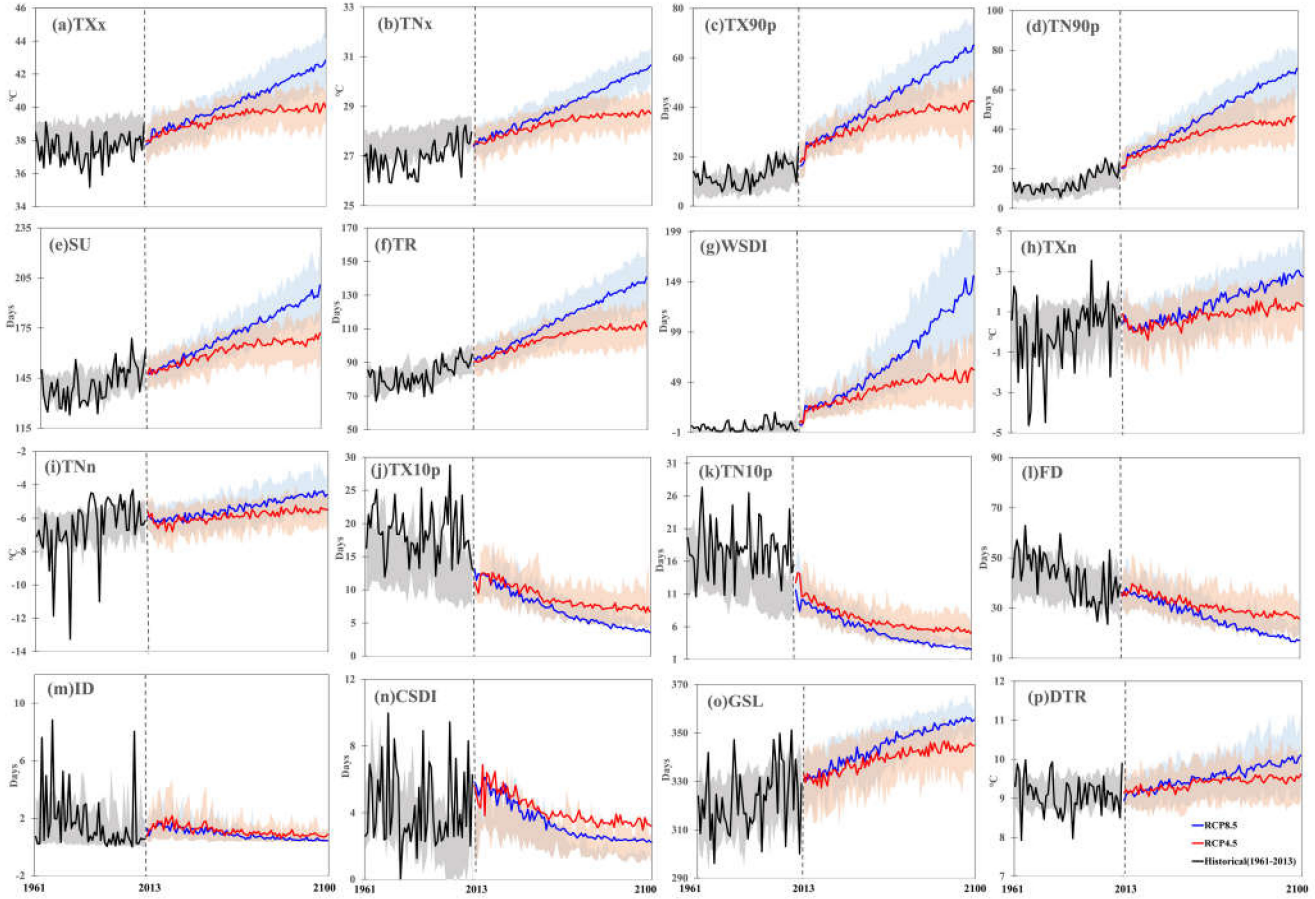

Figure 7. Time series (1961–2100) of the multi-model ensemble simulated extreme temperature indices (**a**, TXx; **b**, TNx; **c**, TX90p; **d**, TN90p; **e**, SU; **f**, TR; **g**, WSDI; **h**, TXn; **i**, TNn; **j**, TX10p; **k**, TN10p; **l**, FD; **m**, ID; **n**, CSDI; **o**, GSL; **p**, DTR) under RCP 4.5 and RCP 8.5 averaged across the HRB. The top and bottom bounds of the shaded area are the 90th and 10th percentile of the annual values, respectively, for the 28 GCM simulation changes in the temperature indices.

4. Discussion

The extreme climate index trends simulated by individual GCMs had large differences with the observations (Figure 2), so the multi-model ensemble featuring 28 GCMs was used to reduce the uncertainties arising from the choice of a single GCM. The close consistency between observations and multi-model ensemble results is expected due to the empirical relationships relied upon by the NWAI-WG statistical downscaling method. Appropriate WGEN parameters are critical for obtaining precise downscale results. Differences can be reduced by the parameters derived from site-specific observations rather than derived directly from coarse-scale GCM.

We found that the HRB has become gradually warmer over the past 50 years and shows a significant increasing trend in the frequency of extreme climate events. These trends are in line with the findings of previous studies carried out in the region during the historical period [35–37]. Our results also showed significant increasing trends in warm extreme indices and decreasing trends for the cold extreme indices over the whole region under RCP4.5 and 8.5. The most significant warming was concentrated in the west and southeast of the HRB, which means that mountainous and populous areas are more vulnerable to climate change than other areas [19,37]. The variation trends of temperature extremes were consistent with the previous results [16,31,33] which projected extreme temperature change over China by using downscaled results from multi-models. However, due to the internal features, the rate of changes in varied regions may differentiate from one another remarkably. For instance, Chen, et al. [31] reported that the five-year ID would disappear during 2071–2100 under RCP8.5 in the lower part of the Yangtze River Basin, whereas in this study, IDwould disappear in 2040s (2021–2060) under RCP4.5 (HRB is in the middle of Yangtze River Basin). The discrepancies are likely attributed to spatial domain differences, which means more details about the regional responses to future temperature extremes are needed.

For spell duration indices, the projections of DTR showed an inconsistent trend during the historical period. The main reasons for these disagreements with observations may be the lack of observations themselves and model biases. The maximum temperature is warming faster than the minimum temperature, so the DTR will significantly increase in the HRB in the future (Table 4). Guan [19] reviewed the IPCC's Fifth Assessment Report (AR5) and considered that the decrease and subsequent increase in DTR may be caused by dimming and subsequent brightening. Sang, et al. [45] suggested that the DTR increase may be related to the impact of urbanization. Nevertheless, as an index highly sensitive to slight changes between maximum and minimum temperatures, there is no consensus on the physical reasons for changes of the DTR, especially for increases of DTR [19]. More studies should be carried out on this issue in the future. GSL showed a significant increase in the future, which is attributed to the recent climate warming in the HRB. The increase in GSL may help increase crop yields by providing opportunities for ensuring maturation, earlier sowing, and multiple cropping [46]. However, the impacts of climate and weather extremes usually result from simultaneous extremes through several variables. Based on this, future analyses of extreme events need to focus on bivariate or multivariate extreme variables.

Extreme temperature changes, such as the decreasing trends of FD and the increasing trends of SU, TXx, and TNn, have the potential to produce a decrease in agricultural productivity. Different crops are sensitive to different extreme indices [17,47,48]. For instance, wheat is very sensitive to increases in warm extreme indices, such as TXx and SU, while barley is sensitive to cold extreme temperature indices, like the decline of FD and the growth of TNn. For rice, an increase of TXx and TNn in the flowering or grain-filling stages, even with short episodes of heat stress, can lead to pollination failure, which can reduce the grain number and yield. In line with a warming trend, there will be more warm days, warm nights, and summer days, with fewer cold days, cold nights, and frost days, in the future. All these results show that the crops in the HRB may sustain more severe heat stress but less frost risk. Countermeasures should thus be taken against extreme temperature changes, such as adjusting the planting distribution and crop-planting structures.

Moreover, the increase in extreme temperature may cause an increase in precipitation and evapotranspiration, leading to the exacerbation of the hydrological cycle, with an associated increase in the frequency and magnitude of torrential rain [6,26,49], and cause the uneven distribution of water resources spatially and seasonally. This study is solely based on annual temperature extremes, without considering the combined effects of other climate variables at seasonal or monthly scales. In India, Revadekar and Preethi [50] found that the effects of extreme precipitation indices may be larger and even more disastrous on grain yield than the extreme temperature indices. Thus, further studies considering changes in extreme precipitation events will be carried out to yield a better understanding of extreme climate changes in the future over the HRB.

5. Conclusions

A multi-model ensemble is an important method to capture and decrease the uncertainties in climate simulations and projections. In this study, we projected the changes of 16 extreme temperature indices based on statistically downscaled site-scale daily temperature data in HRB with multi-model ensembles of 28 GCMs under RCP4.5 and 8.5 scenarios. As indicated by the temporal consistency of the changing trends and small RMSEs (Table 3) between the projected and observed extreme temperature indices (Figure 2), the ensemble extreme temperature indices from downscaled multi-GCM data can represent the patterns of observed values over the whole region. Except for DTR, the extreme temperature indices show uniform patterns on the time scale, with widespread significant increases (TXx, TNx, TXn, TNn, TN90p, TX90p, WSDI, SU, TR, and GSL) and significant decreases (TN10p, TX10p, CSDI, FD, and ID) concurring within the generally expected results of a warming environment. SU, TXx, and TNn, which may increase the frequency, number, and duration of heatwaves in the future, showed particularly strong upwards trends. Further, the changes in TN90p and TN10p were greater than those in TX90p and TX10p during 1961–2013. We found that the changing amplitudes of T-min extremes are greater than those of the T-max extremes, whose means are asymmetric to the changes in temperature extremes in the daytime and nighttime. Furthermore, the growth rate under RCP8.5 is greater than that of RCP4.5. The findings of this research may improve regional strategies for adapting to extreme climate change and scientifically mitigating disasters.

Supplementary Materials: Supplementary materials can be found at http://www.mdpi.com/2073-4433/11/4/424/s1.

Author Contributions: Conceptualization, W.X. and B.W.; methodology, B.W. and D.L.L.; supervision, D.L.L.; data analysis, W.X., B.W., P.F.; writing of original draft preparation, W.X.; writing of review and editing, W.X., B.W., D.L.L. and P.F. All authors have read and agreed to the published version of the manuscript.

Funding: The work was jointly supported by a grant from Shaanxi Province Science and Technology Department project (grant numbers: 2017NY-202) and Shaanxi Province Education Department project (grant numbers: 17JK0014).

Acknowledgments: The authors acknowledge that the Chinese Scholarship Council provided the scholarship and the NSW Department of Primary Industries provided office facilities for conducting this work.

Conflicts of Interest: The authors declare no conflict of interest.

References

1. Field, C.; Barros, V.; Stocker, T. Managing the risks of extreme events and disasters to advance climate change adaptation:Special report of the Intergovernmental Panel on Climate Change. *J. Clin. Endocrinol. Metab.* **2012**, *18*, 586–599.
2. Fischer, E.M.; Knutti, R. Anthropogenic contribution to global occurrence of heavy-precipitation and high-temperature extremes. *Nat. Clim. Chang.* **2015**, *5*, 560–564. [CrossRef]
3. IPCC. *Climate Change 2013: The Physical Science Basis. Fifth Assessment Report of the Intergovernmental Panel Contribution of Working Group on Climate Change*; Cambridge University Press: Cambridge, UK, 2013.
4. Zhang, G.; Dong, J.; Zhou, C.; Xu, X.; Min, W.; Hua, O.; Xiao, X. Increasing cropping intensity in response to climate warming in Tibetan Plateau, China. *Field Crop. Res.* **2013**, *142*, 36–46. [CrossRef]

5. Wang, B.; Liu, D.L.; Macadam, I.; Alexander, L.V.; Abramowitz, G.; Yu, Q. Multi-model ensemble projections of future extreme temperature change using a statistical downscaling method in south eastern Australia. *Clim. Chang.* **2016**, *138*, 85–98. [CrossRef]
6. Allen, M.R.; Ingram, W.J. Constraints on future changes in climate and the hydrologic cycle. *Nature* **2002**, *419*, 228–232. [CrossRef] [PubMed]
7. Easterling, D.R.; Meehl, G.A.; Parmesan, C.; Changnon, S.A.; Karl, T.R.; Mearns, L.O. Climate extremes: Observations, modeling, and impacts. *Science* **2000**, *289*, 2068–2074. [CrossRef] [PubMed]
8. Alexander, L.V.; Zhang, X.; Peterson, T.C.; Caesar, J.; Gleason, B.; Tank, A.M.G.K.; Haylock, M.; Collins, D.; Trewin, B.; Rahimzadeh, F. Global observed changes in daily climate extremes of temperature and precipitation. *J. Geophys. Res. Atmos.* **2006**, *111*, 1042–1063. [CrossRef]
9. Kharin, V.V.; Zwiers, F.; Zhang, X.; Wehner, M. Changes in temperature and precipitation extremes in the CMIP5 ensemble. *Clim. Chang.* **2013**, *119*, 345–357. [CrossRef]
10. Schoof, J.T.; Robeson, S.M. Projecting changes in regional temperature and precipitation extremes in the United States. *Weather Clim. Extrem.* **2016**, *11*, 28–40. [CrossRef]
11. Alexander, L.V.; Arblaster, J.M. Historical and projected trends in temperature and precipitation extremes in Australia in observations and CMIP5. *Weather Clim. Extrem.* **2017**, *15*, 34–56. [CrossRef]
12. Nikulin, G.; Kjellström, E.; Hansson, U.; Strandberg, G.; Ullerstig, A. Evaluation and future projections of temperature, precipitation and wind extremes over Europe in an ensemble of regional climate simulations. *Tellus* **2011**, *63*, 41–55. [CrossRef]
13. Shi, C.; Jiang, Z.-H.; Chen, W.-L.; Li, L. Changes in temperature extremes over China under 1.5 °C and 2 °C global warming targets. *Adv. Clim. Chang. Res.* **2018**, *9*, 120–129. [CrossRef]
14. Tian, J.; Liu, J.; Wang, J.; Li, C.; Nie, H.; Yu, F. Trend analysis of temperature and precipitation extremes inmajor grain producing area of China. *Int. J. Climatol.* **2016**, *37*, 672–687. [CrossRef]
15. Yang, T.; Li, H.; Wang, W.; Xu, C.Y.; Yu, Z. Statistical downscaling of extreme daily precipitation, evaporation, and temperature and construction of future scenarios. *Hydrol. Process.* **2012**, *26*, 3510–3523. [CrossRef]
16. Li, L.; Yao, N.; Li, Y.; Liu, D.L.; Wang, B.; Ayantobo, O.O. Future projections of extreme temperature events in different sub-regions of China. *Atmos. Res.* **2019**, *217*, 150–164. [CrossRef]
17. He, L.; Cleverly, J.; Wang, B.; Jin, N.; Mi, C.; Liu, D.L.; Yu, Q. Multi-model ensemble projections of future extreme heat stress on rice across southern China. *Theor. Appl. Climatol.* **2018**, *133*, 1107–1118. [CrossRef]
18. Kang, L.; Peng, B.; Li, J.; Liu, C. Variability of temperature extremes in the Yellow River basin during 1961–2011. *Quat. Int.* **2014**, *336*, 52–64.
19. Guan, Y.; Zhang, X.; Zheng, F.; Wang, B. Trends and variability of daily temperature extremes during 1960–2012 in the Yangtze River Basin, China. *Glob. Planet. Chang.* **2015**, *124*, 79–94. [CrossRef]
20. Miao, C.; Xi, Y.; Wu, J.; Duan, Q.; Lei, X.; Li, H. Spatiotemporal changes in extreme temperature and precipitation events in the Three-Rivers Headwater region, China. *J. Geophys. Res. Atmos.* **2018**, *123*, 5827–5844.
21. Zhao, Y.; Zou, X.; Cao, L.; Xu, X. Changes in precipitation extremes over the Pearl River Basin, southern China, during 1960–2012. *Quat. Int.* **2014**, *333*, 26–39. [CrossRef]
22. Liu, S.; Huang, S.; Xie, Y.; Qiang, H.; Leng, G.; Hou, B.; Ying, Z.; Xiu, W. Spatial-temporal changes of maximum and minimum temperatures in the Wei River Basin, China: Changing patterns, causes and implications. *Atmos. Res.* **2018**, *204*, 1–11. [CrossRef]
23. Nie, C.J.; Li, H.R.; Yang, L.S.; Ye, B.X.; Dai, E.F.; Wu, S.H.; Liu, Y.; Liao, Y.F. Spatial and temporal changes in extreme temperature and extreme precipitation in Guangxi. *Quat. Int.* **2012**, *263*, 162–171. [CrossRef]
24. Taylor, K.E.; Stouffer, R.J.; Meehl, G.A. An overview of CMIP5 and the Experiment Design. *Bull. Am. Meteorol. Soc.* **2012**, *93*, 485–498. [CrossRef]
25. Zhou, B.; Wen, Q.H.; Xu, Y.; Song, L.; Zhang, X. Projected Changes in Temperature and Precipitation Extremes in China by the CMIP5 Multimodel Ensembles. *J. Clim.* **2014**, *27*, 6591–6611. [CrossRef]
26. Wang, X.; Yang, T.; Li, X.; Shi, P.; Zhou, X. Spatio-temporal changes of precipitation and temperature over the Pearl River basin based on CMIP5 multi-model ensemble. *Stoch. Environ. Res. Risk Assess.* **2017**, *31*, 1077–1089. [CrossRef]
27. Xue, Y.; Vasic, R.; Janjic, Z.; Mesinger, F.; Mitchell, K.E. Assessment of Dynamic Downscaling of the Continental U.S. Regional Climate Using the Eta/SSiB Regional Climate Model. *J. Clim.* **2007**, *20*, 4172–4193. [CrossRef]

28. Guo, J.; Huang, G.; Wang, X.; Li, Y.; Lin, Q. Dynamically-downscaled projections of changes in temperature extremes over China. *Clim. Dyn.* **2018**, *50*, 1045–1066. [CrossRef]
29. Ayar, P.V.; Vrac, M.; Bastin, S.; Carreau, J.; Déqué, M.; Gallardo, C. Intercomparison of statistical and dynamical downscaling models under the EURO- and MED-CORDEX initiative framework: Present climate evaluations. *Clim. Dyn.* **2016**, *46*, 1301–1329. [CrossRef]
30. Wilby, R.L.; Dawson, C.W.; Barrow, E.M. Sdsm—A decision support tool for the assessment of regional climate change impacts. *Environ. Model. Softw.* **2002**, *17*, 145–157. [CrossRef]
31. Chen, Y.D.; Li, J.; Zhang, Q. Changes in site-scale temperature extremes over China during 2071–2100 in CMIP5 simulations. *J. Geophys. Res. Atmos.* **2016**, *121*, 2732–2749. [CrossRef]
32. Li, Z.; Zheng, F.-L.; Liu, W.-Z.; Jiang, D.-J. Spatially downscaling GCMs outputs to project changes in extreme precipitation and temperature events on the Loess Plateau of China during the 21st Century. *Glob. Planet. Chang.* **2012**, *82*, 65–73. [CrossRef]
33. Chen, Y.D.; Li, J.; Zhang, Q.; Gu, X. Projected changes in seasonal temperature extremes across China from 2017 to 2100 based on statistical downscaling. *Glob. Planet. Chang.* **2018**, *166*, 30–40. [CrossRef]
34. Qi, W.; Li, H.; Zhang, Q.; Zhang, K. Forest restoration efforts drive changes in land-use/land-cover and water-related ecosystem services in China's Han River basin. *Ecol. Eng.* **2019**, *126*, 64–73. [CrossRef]
35. Ren, L.; Yin, S. Temperature Changes and its Impacts on Agriculture in the upper Reaches of Hanjiang River in Southern Shaanxi. *Chin. J. Agrometeorol.* **2013**, *34*, 272–277.
36. Zhao, J.; Yang, X.; Xu, Y.; Zhou, Q. Research on the Variation of Extreme Temperature Index in Ankang, Shaanxi in Recent 50 Years. *J. Catastrophol.* **2016**, *31*, 89–94.
37. Xiang, W.; Cheng, Z.; Zhou, B.; Bin, X.; Feng, D. Spatial heterogeneity of temperature extremes in the Qinling-Daba Mountains region in 1975–2016. *Clim. Chang. Res.* **2018**, *14*, 362–370.
38. Liu, W.; Liu, G.; Liu, H.; Song, Y.; Zhang, Q. Subtropical reservoir shorelines have reduced plant species and functional richness compared with adjacent riparian wetlands. *Environ. Res. Lett.* **2013**, *8*, 4007. [CrossRef]
39. Cai, S.; Chen, G.; Du, Y.; Wu, Y. Thoughts on sustainable development in the basin of Hanjiang River. *Resour. Environ. Yangtze Basin* **2000**, *9*, 411–418.
40. Liu, D.L.; Zuo, H. Statistical downscaling of daily climate variables for climate change impact assessment over New South Wales, Australia. *Clim. Chang.* **2012**, *115*, 629–666. [CrossRef]
41. Zhang, H.; Wang, B.; Zhang, M.; Feng, P.; Cheng, L.; Yu, Q.; Eamus, D. Impacts of future climate change on water resource availability of eastern Australia. *J. Hydrol.* **2019**, *573*, 49–59. [CrossRef]
42. Kendall, M.G. *Rank Correlation Methods*; Charles Griffin: London, UK, 1975.
43. Mann, H.B. Nonparametric tests against trend. *Econometrica* **1945**, *13*, 245–259. [CrossRef]
44. Sen, P.K. Estimates of the Regression Coefficient Based on Kendall's Tau. *Publ. Am. Stat. Assoc.* **1968**, *63*, 1379–1389. [CrossRef]
45. Sang, Y.-F.; Wang, Z.; Liu, C. Spatial and temporal variability of daily temperature during 1961–2010 in the Yangtze River Basin, China. *Quat. Int.* **2013**, *304*, 33–42. [CrossRef]
46. Linderholm, H.W. Growing season changes in the last century. *Agric. For. Meteorol.* **2006**, *137*, 1–14. [CrossRef]
47. Hatfield, J.L.; Prueger, J.H. Temperature extremes: Effect on plant growth and development. *Weather Clim. Extrem.* **2015**, *10*, 4–10. [CrossRef]
48. Jagadish, S.; Murty, M.; Quick, W. Rice responses to rising temperatures–challenges, perspectives and future directions. *Plant Cell Environ.* **2015**, *38*, 1686–1698. [CrossRef]
49. Fowler, A.; Hennessy, K. Potential impacts of global warming on the frequency and magnitude of heavy precipitation. *Nat. Hazards* **1995**, *11*, 283–303. [CrossRef]
50. Revadekar, J.V.; Preethi, B. Statistical analysis of the relationship between summer monsoon precipitation extremes and foodgrain yield over India. *Int. J. Climatol.* **2012**, *32*, 419–429. [CrossRef]